

# The physical structure of the point-symmetric and quadrupolar planetary nebula NGC 6309

R. Vázquez<sup>1</sup>, L. F. Miranda<sup>2</sup>, L. Olguín<sup>1,3</sup>, S. Ayala<sup>3,4</sup>,  
J. M. Torrelles<sup>5</sup>, M. E. Contreras<sup>1</sup>, and P. F. Guillén<sup>1</sup>

<sup>1</sup> Instituto de Astronomía, Universidad Nacional Autónoma de México, Apdo. Postal 877, 22800 Ensenada, B. C., Mexico  
e-mail: vazquez, mcontreras, fg Guillen@astro sen. unam. mx

<sup>2</sup> Instituto de Astrofísica de Andalucía, CSIC, P. O. Box 3004, E-18080 Granada, Spain  
e-mail: lfm@iaa.es

<sup>3</sup> Instituto de Astronomía, Universidad Nacional Autónoma de México, Apdo. Postal 70-264, 04510 México, D. F., Mexico  
e-mail: lorenzo@astro sen. unam. mx

<sup>4</sup> Centro de Radioastronomía y Astrofísica, Universidad Nacional Autónoma de México, Apdo. Postal 3-72 (Xangari), Morelia, Mich., Mexico  
e-mail: s. ayala@astro smo. unam. mx

<sup>5</sup> Instituto de Ciencias del Espacio (CSIC) - IEEC, Facultat de Física, Universitat de Barcelona, Av. Diagonal 647, 08028 Barcelona, Spain  
e-mail: torrelles@ieec. fcr. es

Received — / Accepted —

## ABSTRACT

**Aims.** We analyse the point-symmetric planetary nebula NGC 6309 in terms of its three-dimensional structure and of internal variations of the physical conditions to deduce the physical processes involved in its formation.

**Methods.** We used VLA-D  $\lambda$ 3.6-cm continuum, ground-based, and HST-archive imaging as well as long slit high- and low-dispersion spectroscopy.

**Results.** The low-dispersion spectra indicate a high excitation nebula, with low to medium variations of its internal physical conditions ( $10, 600 \text{ K} \lesssim T_e[\text{O III}] \lesssim 10, 900 \text{ K}$ ;  $10, 100 \text{ K} \lesssim T_e[\text{N II}] \lesssim 11, 800 \text{ K}$ ;  $1440 \text{ cm}^{-3} \lesssim N_e[\text{S II}] \lesssim 4000 \text{ cm}^{-3}$ ;  $1700 \text{ cm}^{-3} \lesssim N_e[\text{Cl III}] \lesssim 2600 \text{ cm}^{-3}$ ;  $1000 \text{ cm}^{-3} \lesssim N_e[\text{Ar IV}] \lesssim 1700 \text{ cm}^{-3}$ ). The radio continuum emission indicates a mean electron density of  $\approx 1900 \text{ cm}^{-3}$ , emission measure of  $5.1 \times 10^5 \text{ pc cm}^{-6}$ , and an ionised mass  $M(\text{H II}) \approx 0.07 M_\odot$ . In the optical images, the point-symmetric knots show a lack of  $[\text{N II}]$  emission as compared with similar features previously known in other PNe. A rich internal structure of the central region is seen in the HST images, resembling a deformed torus. Long slit high-dispersion spectra reveal a complex kinematics in the central region, with internal expansion velocities ranging from  $\approx 20$  to  $30 \text{ km s}^{-1}$ . In addition, the spectral line profiles from the external regions of NGC 6309 indicate expanding lobes ( $\approx 40 \text{ km s}^{-1}$ ) as those generally found in bipolar nebulae. Finally, we have found evidence for the presence of a faint halo, possibly related to the envelope of the AGB-star progenitor.

**Conclusions.** Our data indicate that NGC 6309 is a quadrupolar nebula with two pairs of bipolar lobes whose axes are oriented  $\text{PA}=40^\circ$  and  $\text{PA}=76^\circ$ . Equatorial and polar velocities for these two pairs of lobes are  $29$  and  $86 \text{ km s}^{-1}$  for the bipolar system at  $\text{PA}=40^\circ$  and  $25$  and  $75 \text{ km s}^{-1}$  for the bipolar system at  $\text{PA}=76^\circ$ . There is also a central torus that is expanding at  $25 \text{ km s}^{-1}$ . Kinematical age for all these structures is around  $3700$  to  $4000 \text{ yr}$ . We conclude that NGC 6309 was formed by a set of well-collimated bipolar outflows (jets), which were ejected in the initial stages of its formation as a planetary nebula. These jets carved the bipolar lobes in the previous AGB wind and their remnants are now observed as the point-symmetric knots tracing the edges of the lobes.

**Key words.** planetary nebulae: individual: NGC 6309 – ISM: kinematics – ISM: abundances

## 1. Introduction

In spite of all the work that up to now has been done to understand the origin of planetary nebulae (PNe) morphologies and their evolution (e.g., Kwok, Purton & FitzGerald 1978; Kahn & West 1985; Balick 1987; Icke 1988; Mellema 1995; Perinotto et al. 2004; Rijkhorst, Mellema & Icke 2005; Schönberner et al. 2005; Schönberner et al. 2007), some morphological structures still remain as unsolved problems. In particular, the so-called point-symmetry (Stanghellini, Corradi & Schwarz, 1993; Gonçalves et al. 2003) appears enigmatic. Some observational studies about point-symmetric PNe (e.g. Miranda & Solf 1992; López, Meaburn & Palmer 1993) relate the formation of these

objects to collimated outflows from a precessing central source known as bipolar rotating episodic jets (BRETs, see López, Vázquez & Rodríguez 1995). However, in some cases, there are not definite proofs about the jet nature of these features as they are not confirmed by spectroscopic studies (e.g. Vázquez et al. 1999a, Vázquez et al. 2002). Although some theoretical models have intended to explain point-symmetric PNe (e.g., Cliffe et al. 1995; Livio & Pringle 1996, 1997; García-Segura & López 2000; Rijkhorst, Icke & Mellema 2004), the origin and shaping of this kind of objects remains a puzzle.

NGC 6309 is a PN whose morphology strongly suggests a BRET scenario for its origin, as can be seen in the  $\text{H}\alpha$ + $[\text{N II}]$  and  $[\text{O III}]$  images by Schwarz, Corradi & Melnick (1992). It has two prominent, point-symmetric ‘arms’ formed by pairs of condensations in addition to a bright internal elliptical structure. Some

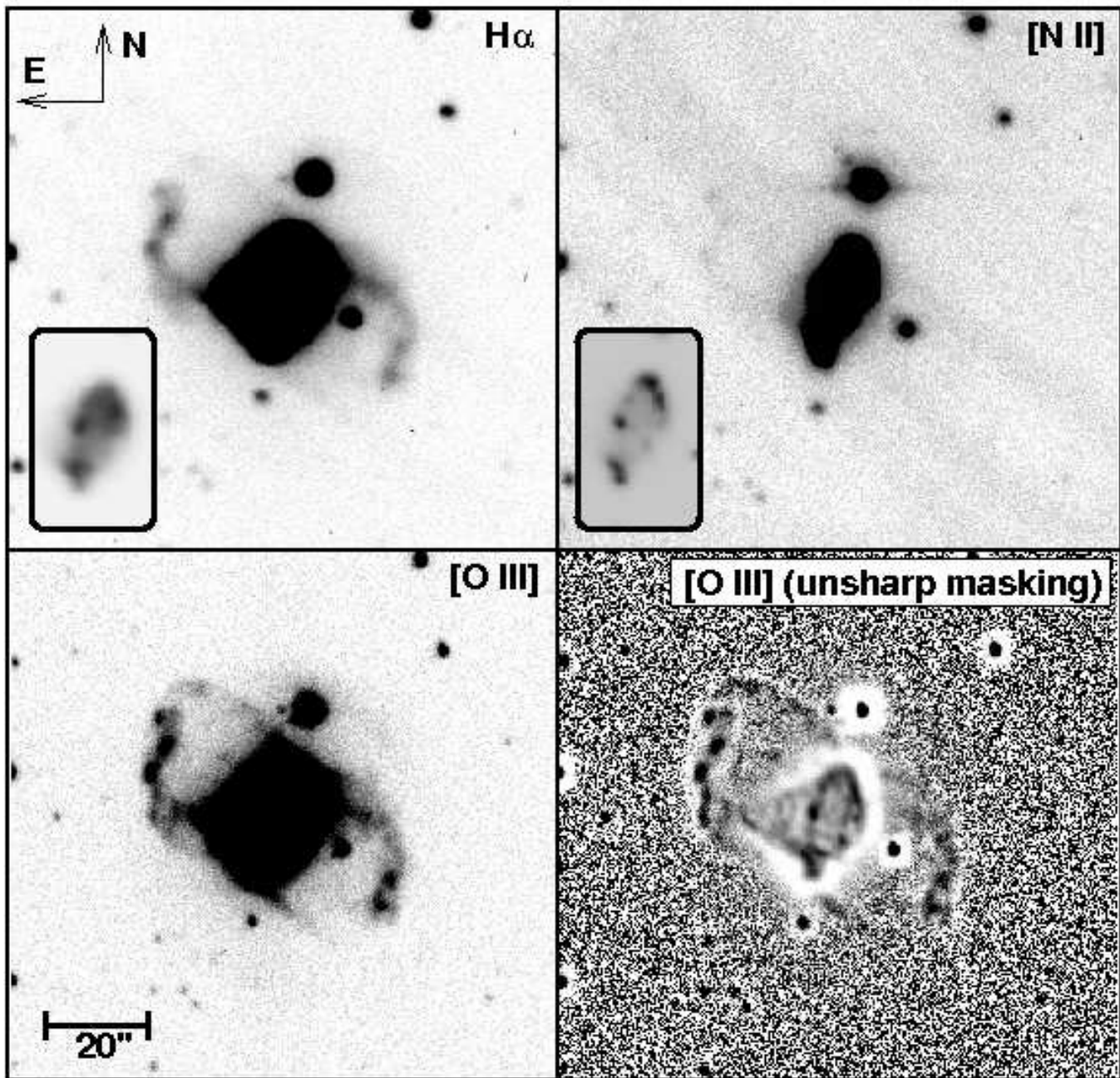


**Fig. 1.** Images of NGC 6309 in the light of  $H\alpha$  (top left),  $[N II]$  (top right) and  $[O III]$  (bottom left), including an unsharp masking of the  $[O III]$  image (bottom right). North is up and east is left in all the panels. Small frames are included inside the upper panels to show the structure of the central region.

previous studies on NGC 6309 have determined an expansion velocity  $V_{\text{exp}}[O III]=34 \text{ km s}^{-1}$  (Sabbadin 1984), as well as mean physical parameters and total abundances (Górny et al. 2004), namely, electron density and temperature  $N_e[S II]=2600 \text{ cm}^{-3}$ ,  $T_e[N II]=12,097 \text{ K}$ ,  $T_e[O III]=11,845 \text{ K}$ ; and abundance ratios  $He/H=0.1$ ,  $N/H=8.20$ ,  $O/H=8.64$ ,  $Ne/H=7.82$ , and  $S/H=6.49$  ( $\log H=12$ , except for  $He/H$  ratio). Armour & Kingsburgh (2001) found similar values. NGC 6309 has also been included in the list of PNe with low ionisation structures (LIS) by Gonçalves et al. (2003). Finally, the central star of NGC 6309 has been classified as a “weak emission line star” by Górny et al. (2004).

In spite of this suggestive morphology, an internal kinematic study of NGC 6309, as well as a full analysis of the physical conditions in the different nebular regions, has not yet been

done. In this paper, we have carried out a radio-optical study of NGC 6309, including radio continuum mapping, optical imaging, and long-slit optical spectroscopy, in both, high- and low-dispersion. We discuss our results on the morphology, kinematics, physical conditions, ionic abundances, and nature of the gas emission to explore the possible mechanisms involved in the formation of NGC 6309.

## 2. Observations and results

### 2.1. CCD ground-based imaging

We obtained narrow-band direct images with the Calar Alto Faint Object Spectrograph (CAFOS) in the 2.2 m telescope at

Calar Alto Observatory (CAHA<sup>1</sup>) in 1998 July 8. We used two filters centered in H $\alpha$  ( $\Delta\lambda = 15\text{\AA}$ ) and [N II]6583 ( $\Delta\lambda = 20\text{\AA}$ ) as well as a CCD Loral with  $2048 \times 2048$  pixels. The exposure time for both images was 1800 s. The scale was  $0''.33 \text{ pixel}^{-1}$  and the seeing was about  $1''.7$ . We obtained an additional image on 2004 August 3 with the 1.5 m telescope at the Observatorio de Sierra Nevada<sup>2</sup>. The detector was a RoperScientific VersArray CCD with  $2048 \times 2048$  pixels, each of  $0''.232 \text{ pixel}^{-1}$ . We used an [O III]5007 ( $\Delta\lambda = 50\text{\AA}$ ) filter with an exposure time of 900 s. The images were reduced following standard procedures within the MIDAS package. In this case, seeing was  $1''.3$ .

Figure 1 shows the images of NGC 6309 in H $\alpha$ , [N II] and [O III]. An additional unsharp masking [O III] image is also presented in Fig. 1 to show the link between internal and external nebular structures. In these images, the high contrast between the brightness of the central region and that of the ‘arms’ is evident. In particular, the lack of emission of [N II] from the ‘arms’ is unexpectedly remarkable given that, in general, this kind of point-symmetric microstructures is related to LIS (Gonçalves et al. 2003). However, there are also some cases in which the emission of [N II] is marginal (e.g. IC 5217; Miranda et al. 2006). In the case of NGC 6309, the lack of [N II] from the point-symmetric knots indicates that these cannot be considered as LIS.

The structure of the ‘arms’ consists of at least four pairs of point-symmetric knots, some of them clearly extended perpendicular to their corresponding radial vector from the central star. The central region of the NGC 6309 is a bright ellipse (major axis  $\approx 20''$ , PA  $-14^\circ$ ) embedded in the main body of the nebula. The arms appear to leave from the vertexes of this ellipse. The unsharp masking [O III] image also shows a conelike structure with its base located on the central ellipse and the vertex on the NE arm. In [O III], faint emission connects the arms with the bright ellipse and seems to trace asymmetrical lobes. In fact, the appearance of NGC 6309 in [O III] resembles that of a quadrupolar PN in which one of the outflows (at PA  $40^\circ$ ) protrude into the lobes of the other (at PA  $76^\circ$ ). Part of the SW lobe appears to be open. Finally, a circular faint halo (probably spherical) is detected in [O III] image (Figs. 1 and 2). Its center coincides with the central star of the nebula and its size is  $\approx 56''$ .

In Fig. 2, we show the unsharp masking [O III] image and label some morphological features that will be discussed later. Knots in the NE arm are named **E1**, **E2**, **E3**, and **E4**, whereas those in the SW arm are named **W1**, **W2**, **W3**, and **W4**. Regions in the ellipse are called **R1** and **R2** for the tips of its major axis, and **R3** and **R4** for those along the minor axis.

## 2.2. HST-WFPC2 imaging

An Hubble Space Telescope (HST) broadband image from the MAST Archive<sup>3</sup> was used in order to improve the general view of the internal morphology of NGC 6309 (proposal ID: 6119; PI: H. E. Bond; Date of observation: 1995 August 26). Figure 3

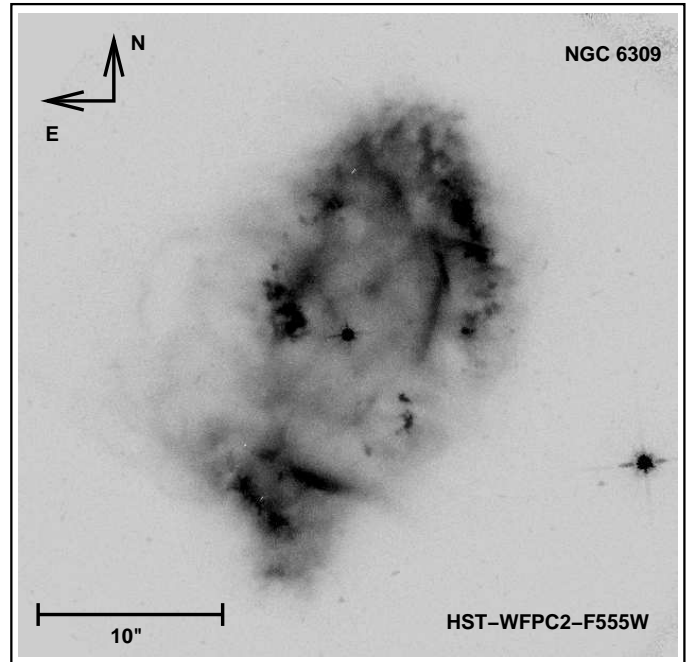


**Fig. 3.** HST broad-band CCD image of NGC 6309 in the filter F555W.

shows the 140 sec image using the filter F555W (nearly Johnson V). This image can be compared with the optical ground-based images in Fig. 1. The bright ellipse is formed by many clumps as well as diffuse gas. The ellipse is open in its SW and SE regions, whereas an apparently double structure is observed in the S and N regions. In addition, a system of faint bubbles is detected towards the NE, which is probably related to the cone-like structure seen in [O III] (see above). Given the short exposure time of the HST image, evidence of the ‘arms’ is very marginal.

## 2.3. $\lambda 3.6$ -cm VLA-D

We obtained radio continuum observations at  $\lambda 3.6$ -cm, toward NGC 6309 with the Very Large Array (VLA) of the National Radio Astronomy Observatory (NRAO)<sup>4</sup> in the D configuration during 1996 August 8. The standard VLA continuum mode with a 100 MHz bandwidth and two circular polarizations was employed. The flux and phase calibrators were 1331 + 305 (adopted flux density 5.2 Jy) and 1733 - 130 (observed flux density 10.7 Jy), respectively. We set phase center at  $\alpha(2000) = 17^{\text{h}}14^{\text{m}}03^{\text{s}}.6$ ,  $\delta(2000) = -12^{\circ}54'37''$ . The on-target integration time was 28 min. We calibrated the data and processed it using standard procedures of the Astronomical Image Processing System (AIPS) package of the NRAO. We obtained a cleaned map of NGC 6309 using the task IMAGR of AIPS (parameter ROBUST = -3; Briggs 1995). Self-calibration was also performed resulting in a final synthesized beam of  $13''.9$  in diameter and rms noise of the map of  $\sigma = 33 \mu\text{Jy beam}^{-1}$ .

The detected radio continuum emission is related to the central region and appears partially resolved. Based on a 2-D Gaussian fit (task IMFIT in AIPS), we estimate a size of  $\approx 19'' \times 16''$  at PA =  $-27^\circ$  (see Fig. 4). The position of the intensity peak was found at  $\alpha(2000) = 17^{\text{h}}14^{\text{m}}04^{\text{s}}.28$ ,  $\delta(2000) = -12^{\circ}54'37''$ .

<sup>1</sup> The Centro Astronómico Hispano-Alemán (CAHA) at Calar Alto, is operated jointly by the Max-Planck Institut für Astronomie and the Instituto de Astrofísica de Andalucía (CSIC).

<sup>2</sup> The Observatorio de Sierra Nevada is operated by the Consejo Superior de Investigaciones Científicas through the Instituto de Astrofísica de Andalucía (Granada, Spain)

<sup>3</sup> Some of the data presented in this paper were obtained from the Multimission Archive at the Space Telescope Science Institute (MAST). STScI is operated by the Association of Universities for Research in Astronomy, Inc., under NASA contract NAS5-26555. Support for MAST for non-HST data is provided by the NASA Office of Space Science via grant NAG5-7584 and by other grants and contracts.

<sup>4</sup> The National Radio Astronomy Observatory is a facility of the National Science Foundation operated under cooperative agreement by Associated Universities, Inc.

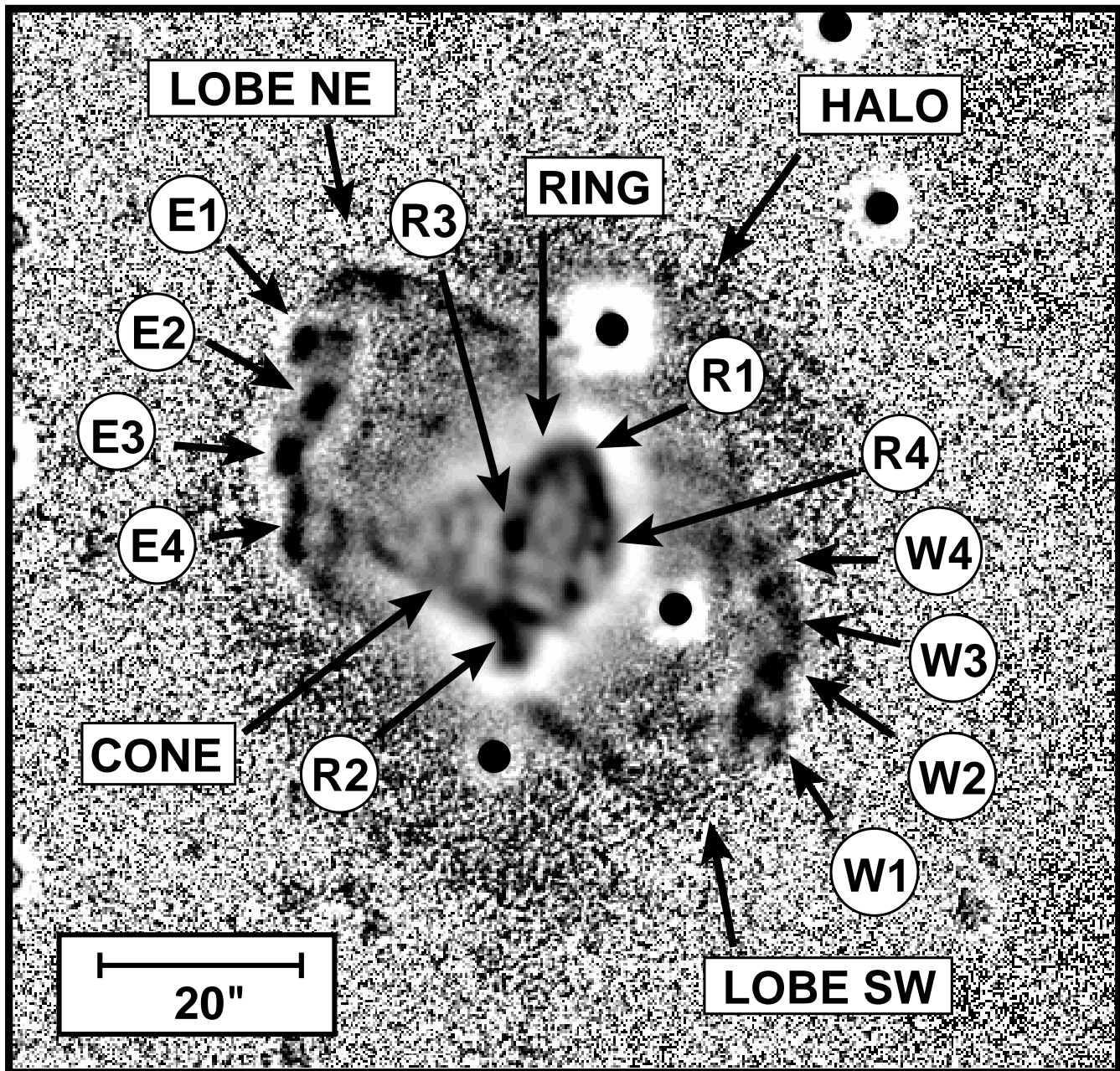


**Fig. 2.** Unsharp-masking image of NGC 6309 in the light of [O III]. North is up and east is left. Main morphological features as well as some regions of particular interest are pointed out and labeled.

The total flux density from the radio map is  $\approx 115$ -mJy, which is similar to those measured by Milne & Aller (1982); Ratag & Pottasch (1991); and Condon & Kaplan (1998); at 2 cm (146-mJy); 6 cm (102-mJy); and 21 cm (132-mJy); respectively. We did not detect emission from the ‘arms’.

We also derived the mean physical conditions, based on the formalism of Mezger & Henderson (1967). Optically-thin emission and  $T_e = 10,000$  K were assumed, obtaining the following results:  $N_e = 1900 \text{ cm}^{-3}$ ;  $M(\text{H II}) = 0.07 M_\odot$ ;  $EM = 5.1 \times 10^5 \text{ pc cm}^{-6}$ . We assumed distance to the nebula to be 2 kpc as the average value from the different estimates, which range between 1.1 and 2.5 kpc (e.g., Daub 1982, Phillips & Pottasch 1984, Amnuel, et al. 1984, Maciel 1984, Cahn, Kaler & Stanghellini, 1992).

#### 2.4. Long slit low-dispersion spectroscopy

Low-dispersion optical spectra were obtained with the Boller & Chivens spectrometer in the 2.1 m UNAM telescope at the San Pedro Mártir Observatory (OAN-UNAM) in 1999 July 19-20 (grating of 300 lines/mm) and 2002 August 7-8 (grating of 400 lines/mm). In all of these cases, a CCD Tek 1024  $\times$  1024 was used as detector. We set the slit width to  $220 \mu\text{m}$  ( $1.6''$ ). The spatial scale is  $1''.05 \text{ pixel}^{-1}$  whereas the spectral scale is 3 and  $4 \text{ \AA pixel}^{-1}$  for the gratings of 400 and 300 lines/mm, respectively. We set the slit at several position angles, which are labeled as C, J, K, L (grating of 300 lines/mm), and A, C, and E (grating of 400 lines/mm), in Fig. 5.

Table 1 shows the dereddened spectra (considering case B of recombination) and physical conditions obtained with the Five-

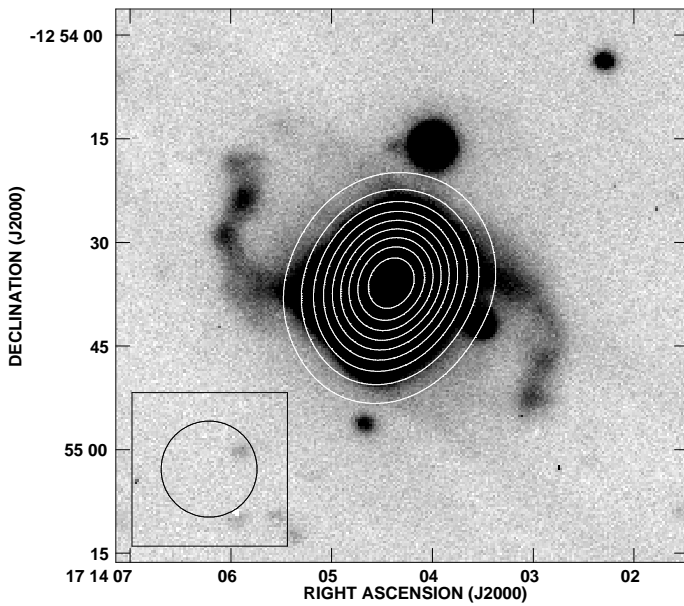


**Fig. 4.** Contour plot  $\lambda$ 3.6-cm continuum map of NGC 6309, overimposed on a  $H\alpha$  image. Contour levels are 10, 20, 30, 40, 50, 60, 70, 80, and 90% of the peak flux ( $6.3 \times 10^{-3}$  Jy). The half-power beam width ( $13''.9$  in diameter) is shown in the bottom-left corner.

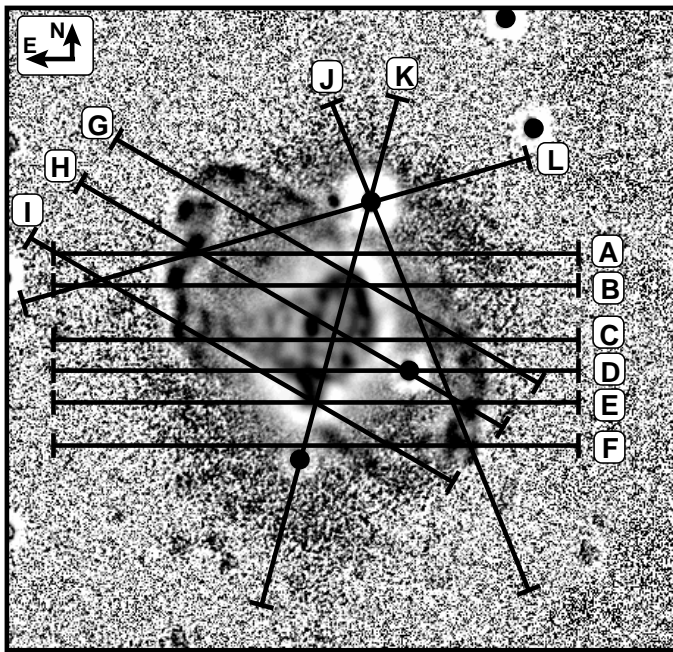


**Fig. 5.** Slits used in spectroscopy overlaid on  $[O\text{ III}]$  unsharp masking image.

Level Atom Diagnostics Package (*nebular*) from IRAF<sup>5</sup> (applying the extinction law by Howarth 1983 for dereddening) for the regions **R1**, **R2**, **R3**, **R4**, **E2**, **W1**, and **W1**.

Physical conditions can only be determined for the regions of the central ellipse. Electron temperature and densities obtained from the high-excitation emission lines appears

<sup>5</sup> The Image Reduction and Analysis Facility (IRAF) is distributed by the National Optical Astronomy Observatories, which are operated by the Association of Universities for Research in Astronomy, Inc., under cooperative agreement with the National Science Foundation.

to be quite uniform ( $T_e[O\text{ III}]=10\,750$  K,  $N_e[Cl\text{ III}]=2350$  cm<sup>-3</sup>,  $N_e[Ar\text{ IV}]=1430$  cm<sup>-3</sup>), with variations within the estimated uncertainties. However, those physical parameters obtained from low-excitation emission ions appear as separated in two different regimes ( $T_e[N\text{ II}]=10\,200$  K, and  $11\,800$  K;  $N_e[S\text{ II}]=1620$  cm<sup>-3</sup> and  $3800$  cm<sup>-3</sup>).

The dereddened absolute  $H\beta$  flux values from regions **R1**, **R2**, **R3**, and **R4** are similar (see Table 1). However, the corresponding logarithmic extinction coefficients  $c_{H\beta}$  spread from 0.70 to 0.97 (mean value including all regions is 0.87), probably due to differences in the internal dust distribution, as has been found in other PNe (e.g. Vázquez et al. 1999b, Lee & Kwok 2005).

In addition, we present the more common ratios for plasma diagnostics at the bottom of Table 1, which show that these regions are emitting by photoionisation-recombination processes with minimal or nonexistent shock-cooling contributions. This could be expected in the surroundings of a hot luminous star, however there are several cases of PNe in which shock-cooling processes make an important contribution to the microstructures emission (see Gonçalves 2003 for a compilation). For comparison, previous spectroscopic studies of NGC 6309 by Górný et al. (2004) give values of  $c(H\beta) \approx 0.88$ ,  $T_e([O\text{ III}]) \approx 11\,845$  K,  $T_e([N\text{ II}]) \approx 12\,097$  K, and  $N_e([S\text{ II}]) \approx 2\,600$  cm<sup>-3</sup>.

We have also estimated ionic and elemental abundances for some regions using IRAF and the ICF (*Ionisation Correction Factors*) method (Kingsburgh & Barlow 1994), although we are aware that recently, Gonçalves et al. (2006) have noticed that elemental abundances derived by using this method are overestimated if they are obtained from narrow, long-slit spectra. The results are shown in Tables 2 and 3.

Regions **R1** and **R2** are similar in physical conditions as well as in ionic abundances. In both regions, the abundances of the three species of oxygen as well as  $He^+$ ,  $Ar^{+2}$ ,  $N^+$ ,  $S^+$ , and  $Cl^{+2}$  are enhanced with respect to the other regions. The opposite occurs for  $Ar^{+3}$  and  $He^{+2}$ .

With reference to elemental abundances, these are consistent with the mean values for PNe and Type I PNe, within uncertainties (see Table 3). The exception is N, which show a deficiency, more in agreement with less-evolved objects, but consistent with previous estimates (Armour & Kingsburgh 2001). Given the values of these abundances, NGC 6309 would be a Type II PN (intermediate population), according to the classification of Peimbert (1978). This is reinforced by the low N/O ratio, which is in agreement with the expected value for a low-mass central star ( $0.6 M_{\odot}$ , according to Kwok 2000). If this interpretation of the abundances is right, NGC 6309 would represent another case of a non-Type I PN with bipolar outflows (see Vázquez et al. 1999a). This strengthens the idea pointed out by Vázquez et al. that some low-mass central stars may also develop bipolar morphologies, in contrast to the fact that bipolar PNe are usually associated with relatively massive central stars (Corradi & Schwarz 1995).

## 2.5. Long slit high-dispersion spectroscopy

We obtained high-dispersion optical spectra with the Manchester Echelle Spectrometer (MES) in the 2.1 m telescope ( $f/7.5$ ) at the San Pedro Mártir observatory (OAN-UNAM) during the period of 2001 May 22-23. We used a CCD SITE with  $1024 \times 1024$  pixels was used as detector, and set the slit width to  $150\text{-}\mu\text{m}$  ( $1.6''$ ). A  $2 \times 2$  binning was used, resulting in a spatial scale of  $0''.6$  pixel<sup>-1</sup> and a spectral scale of  $0.1 \text{ \AA}$  pixel<sup>-1</sup>. We centered

the spectral range at the  $H\alpha$  emission line. The spectra were wavelength calibrated with a Th-Ar arc lamp to an accuracy of  $\pm 2 \text{ km s}^{-1}$ . The achieved spectral resolution, as indicated by the FWHM of the comparison lines, was  $12 \text{ km s}^{-1}$ . Several spectra were obtained with the slit oriented E-W (slits A to F on Fig. 5).

We obtained on 2004 July 29-30, a second series of spectra, using the same telescope and instrument. In this case, the spectra were centered on the  $[\text{O III}] \lambda 5007$  emission line (slits G, H, I, and K on Fig. 5), and the spectral scale was  $0.08 \text{ \AA pixel}^{-1}$ .

Position-velocity (PV) maps for the  $H\alpha$  and  $[\text{O III}] \lambda 5007$  are shown in Fig. 6. We note that the  $\text{He II} \lambda 6560$  line is also observed in the PV maps at the slits B, C, and D. In the PV maps (Fig. 6) relative position is measured with respect to the central star whereas radial velocity is measured relative to the systemic velocity, for which we deduce  $V_{\text{LSR}} = -32 \pm 2 \text{ km s}^{-1}$ , based on the expansion velocity at the position of the central star ( $[\text{O III}]$  spectra from slits H and K). This value is close to that reported by Schneider et al. (1983) of  $V_{\text{LSR}} \simeq -33.4 \pm 2.8 \text{ km s}^{-1}$ .

In a first step to analyse the high-resolution spectra, we extract from the PV maps the spatial position and radial velocity of the individual regions labeled in Fig. 2. The results are listed in Table 4. The knots in the arms present a noticeable point-symmetry, both in their position with respect to the central star and in their radial velocity. In the case of the regions in the bright ellipse, **R1** and **R2** are moving at the systemic velocity while **R3** and **R4**, located along the minor axis, present the maximum radial velocity in this structure.

In a second step, we analyse the emission-line features in the PV maps as a whole. Slits H and K are tracing the minor and major axes of the internal ellipse, respectively. In the PV map of slit H (Fig. 6), the regions **E2** and **W2** can be noted as bright condensations located at the extremes of the emission-line features. Maximum expansion velocity at the lobes can be measured as  $2v_{\text{exp}} \simeq 80 \text{ km s}^{-1}$  (SW lobe expansion is best viewed in panel I). The lobe NE shows a bulk radial velocity of  $\simeq +20 \text{ km s}^{-1}$  (as measured at  $20''$  from the center, panel H), whereas the lobe SW presents  $\simeq -20 \text{ km s}^{-1}$  (as measured at  $20''$  from the center, panel I). The central region also seems to be expanding, showing a maximum velocity splitting of  $2v_{\text{exp}} \simeq 69 \pm 2 \text{ km s}^{-1}$ , making it difficult to determine the radial velocity of the microstructures **R3** and **R4** accurately. However, the PV map from slit H ( $[\text{O III}]$ ) shows evidence of two additional components separated  $\simeq 8''$  and  $\simeq 46 \text{ km s}^{-1}$  that could be these features (locations are indicated on Fig. 6 by a pair of arrows).

Slit K crosses the major axis of the ellipse. In the corresponding PV map, a velocity ellipse is observed. Features **R1** and **R2** move with the systemic velocity. However, small regions beyond the ellipse are also found with radial velocities of  $\simeq \pm 30 \text{ km s}^{-1}$ . Maximum expansion velocity is observed at the center of the ellipse ( $2v_{\text{exp}} \simeq 66 \pm 2 \text{ km s}^{-1}$ ), which is nearly compatible with previous spectroscopic studies (Sabbadin 1984,  $\simeq 68 \pm 3 \text{ km s}^{-1}$ ; Armour & Kingsburgh 2001,  $\simeq 64 \pm 5 \text{ km s}^{-1}$ ).

From these slits (H and K), the presence of two expanding asymmetrical lobes and a velocity ellipse in the center is evident. The expansion of these bipolar lobes is confirmed with data from the other slits, and the kinematics of their borders is traced by that of the point-symmetric knots.

In the PV map from slit A, we detect an intense emission centered at  $2''$  toward the west and relative velocity centered at  $V_r \simeq +20 \text{ km s}^{-1}$ . This feature corresponds to the upper border of the ellipse ( $\simeq 5''$  above **R1**). Faint emission from the halo is detected to the west of this feature (up to  $\simeq 10'' - 25''$ ) in agreement with the observed size of this structure.

**Table 4.** Basic kinematical data for the main morphological features in NGC 6309. Angular distance and position angle (PA) are measured from the central star. Radial velocity is measured with respect to the systemic velocity ( $-32 \text{ km s}^{-1}$ ) from the emission line indicated in the last column. Uncertainties for the first row apply to the rest.

| Feature   | PA<br>( $^\circ$ ) | Angular<br>distance<br>( $''$ ) | Radial<br>velocity<br>( $\text{km s}^{-1}$ ) | Emission<br>line             |
|-----------|--------------------|---------------------------------|--|------------------------------|
| <b>R1</b> | $-15 \pm 4^\circ$  | $9 \pm 3''$                     | $0 \pm 2 \text{ km s}^{-1}$                  | $[\text{O III}]$             |
| <b>R2</b> | $+165$             | 10                              | 0  | $[\text{O III}]$             |
| <b>R3</b> | $+75$              | 4                               | $+23$  | $[\text{O III}]$             |
| <b>R4</b> | $-105$             | 4                               | $-23$  | $[\text{O III}]$             |
| <b>E1</b> | $+50$              | 30                              | $+35$  | $[\text{O III}]$             |
| <b>E2</b> | $+60$              | 26                              | $+36$  | $H\alpha$ , $[\text{O III}]$ |
| <b>E3</b> | $+70$              | 27                              | $+35$  | $H\alpha$                    |
| <b>E4</b> | $+90$              | 25                              | $+24$  | $H\alpha$                    |
| <b>W1</b> | $-130$             | 27                              | $-34$  | $H\alpha$                    |
| <b>W2</b> | $-120$             | 25                              | $-36$  | $H\alpha$ , $[\text{O III}]$ |
| <b>W3</b> | $-110$             | 24                              | $-34$  | $H\alpha$ , $[\text{O III}]$ |
| <b>W4</b> | $-90$              | 21                              | $-20$  | $H\alpha$                    |

On the other hand, the PV map of slit I shows the radial velocity of feature **E4** (the brightest feature) as  $\simeq +24 \text{ km s}^{-1}$ , in addition to the expansion velocity of lobe SW close to  $\simeq 40 \text{ km s}^{-1}$ . Finally, the PV map of slit C covers the region at lobe NE corresponding to the cone-like structure. This region expands to  $\simeq 25 \text{ km s}^{-1}$ , and is located from  $5''$  to  $15''$  toward the East from the center. The kinematics of the cone is practically indistinguishable from that of lobe NE.

### 3. Discussion

#### 3.1. The physical structure of NGC 6309

The most reasonable explanation for the morphology and kinematics of the central ellipse is that such structure corresponds to a tilted expanding torus. Although other possible structures are possible, this interpretation appears to be a better fit to our data. Assuming that the torus is circular and its diameter is  $\simeq 20''$ , we deduce an inclination angle of the torus axis with respect to the line of sight of  $66^\circ$ . The expansion velocity of the torus, corrected by the inclination angle is  $V_{\text{exp}} \simeq 25 \text{ km s}^{-1}$ . Therefore, the size of this structure and its kinematic age are  $\simeq 0.2 \text{ pc}$  and  $3800 \text{ yr}$  respectively, assuming a distance of  $2 \text{ kpc}$ . In addition, the northeastern half of the torus is blueshifted whereas the southwestern half is redshifted. We note that these calculations have been obtained from the earth-based observations. Since the HST image shows a more complex structure in the torus, these results should be considered as an approximation only.

With regard to the bipolar lobes, it is clear that a model of a single bipolar system with a main axis cannot reproduce the observed morphology, given the apparent two directions observed in the nebula. Therefore, we have considered a quadrupolar model consisting of two pairs of bipolar lobes, one of them oriented at  $\text{PA} +76^\circ$ , coincident with the torus axis, and the other at  $\text{PA} +40^\circ$ , coinciding with the apparent protrusions in the lobes along this axis. Each of these bipolar systems is described following the formulation by Solf & Ulrich (1985),

$$V(\phi) = V_e + (V_p - V_e) \times \sin^\alpha(|\phi|), \quad (1)$$

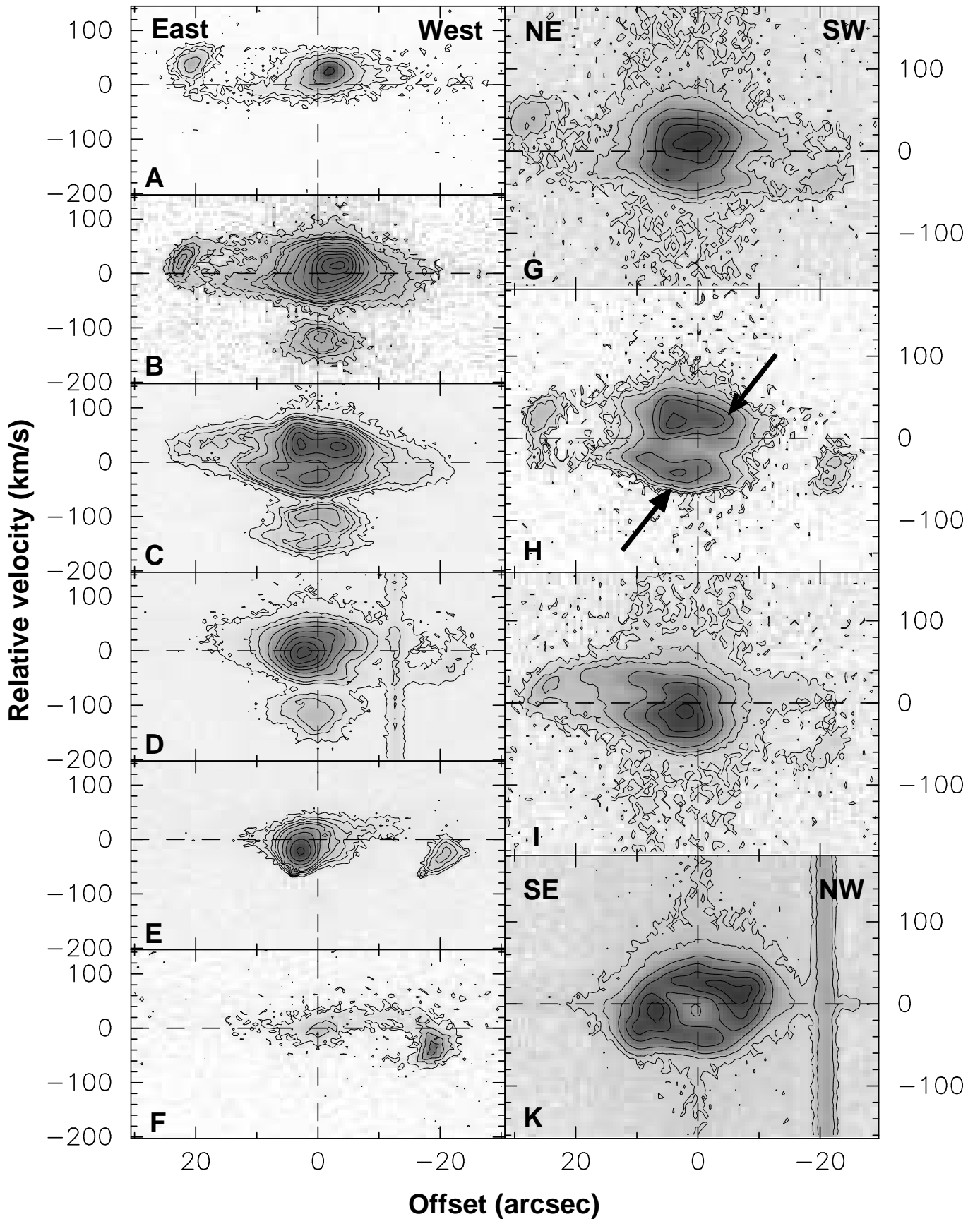


**Fig. 6.** Position-velocity gray/contour maps corresponding to the slits A to F in the light of  $H\alpha$  (left panels), and slits G, H, I, and K in  $[O\text{ III}]\lambda 5007$  (right panels). Slit orientation is indicated, being the same for all the left panels. In the right panels orientation is indicated on panels for slits G (valid also for H and I) and K. Velocity scale is different in left and right panels. The vertical dashed lines represent the projected position of the central star perpendicular to the corresponding slit position. On each panel, the horizontal dashed line corresponds to the systemic radial velocity ( $V_{\text{LSR}} = -32 \pm 2 \text{ km s}^{-1}$ ). Arrows in panel H indicate location of two features explained in the text.

where  $\phi$  is the latitude angle above the equator;  $V_e$  and  $V_p$  are the equatorial and polar expansion velocity respectively; and  $\alpha$  is an exponent that fits the specific hour-glass shape. With the main assumption that the axis of the torus and that of the bipolar ejection at PA +76° are the same, the kinematics and morphology of this outflow can be reasonably reproduced with  $V_e = 25 \text{ km s}^{-1}$  (expansion velocity of the torus),  $V_p = 75 \text{ km s}^{-1}$ , and  $\alpha = 6$ . There is no clue about the inclination angle of the outflow at PA +40°. If we assume the same inclination angle, we find reasonable fits for this bipolar system with  $V_e = 29 \text{ km s}^{-1}$ ,  $V_p = 86 \text{ km s}^{-1}$ , and  $\alpha = 6$ . In Fig. 7, we show the hour-glass shapes deduced from these fits overlaid on the unsharp-masking image of NGC 6309. The observed shape, as well as the kinematics of the knots, are reasonably reproduced by the models. With the model data and the assumption of a distance of 2 kpc, we find a kinematical age of 4 000 yr for the bipolar lobes at PA +40° and of 3700 yr for the bipolar system at PA +76°. These ages are not very different from each other and are also similar to the age deduced for the torus. This suggests that the formation of the different structures in NGC 6309 has occurred in a relatively small time span. In addition, as these kind of outflows have been observed in proto-planetary nebulae (PPN, e.g. Sahai 1998), our results impose a minimal value of time ( $\approx 4000 \text{ yr}$ ) for the PPN to PN stage in this nebula. Other structures such as the “cone” and the halo, are present in this nebula, but we must conduct further studies to understand their physical properties.

### 3.2. The formation of NGC 6309

The appearance of NGC 6309, as well as the position of the point-symmetric knots perpendicular to a radial position vector from the central star, strongly resemble the point-symmetric structures observed in Fleming 1 (López et al. 1993). Cliffe et al. (1995) studied the interaction of a precessing jet with the interstellar medium. They find that point-symmetric structures can be formed by this interaction, and with the time, the individual bow-shocks can merge into a single shock structure. The ulterior evolution of such structures will lead to the formation of bipolar lobes with non-uniform brightness distribution being point-symmetric respect to the central star. On the other hand, García-Segura & López (2000) made models of bipolar PN with point-symmetric structures using a steady misalignment of the magnetic collimation axis with respect to the symmetry axis of the bipolar outflow. In their models, such morphology is also produced by the action of jets.

A possible scenario for the formation of NGC 6309 is that the knots are the remnants of high-velocity bipolar collimated outflows that were ejected in the proto-planetary nebula (PPN) stage. There is evidence that precessing jets in young proto-PN carve bipolar or multipolar cavities in the initial stage of PNe evolution (e.g. Sahai & Trauger 1998, Sahai et al. 2005, Sánchez-Contreras et al. 2006). In such a scenario, the precessing jet is ejected during the proto-PN phase and after that, subsequently, it is stopped and cooled by its surroundings. The knots follow the thermal expansion of the bipolar lobes. In this case, the brightness of the knots comes mainly from the photoionisation process, as the shocked-cooled emission has turned off or it is hidden by the effect of a high-excitation photon source. This could explain the lack of [N II] emission in the point-symmetric knots.

In addition, we constructed a [O III]/H $\alpha$  ratio image from images in Fig. 1. Such ratio image can be used as a diagnostic tool, as has been shown by Medina et al. (2007). Figure 8 shows the [O III]/H $\alpha$  ratio image in which an enhancement of the

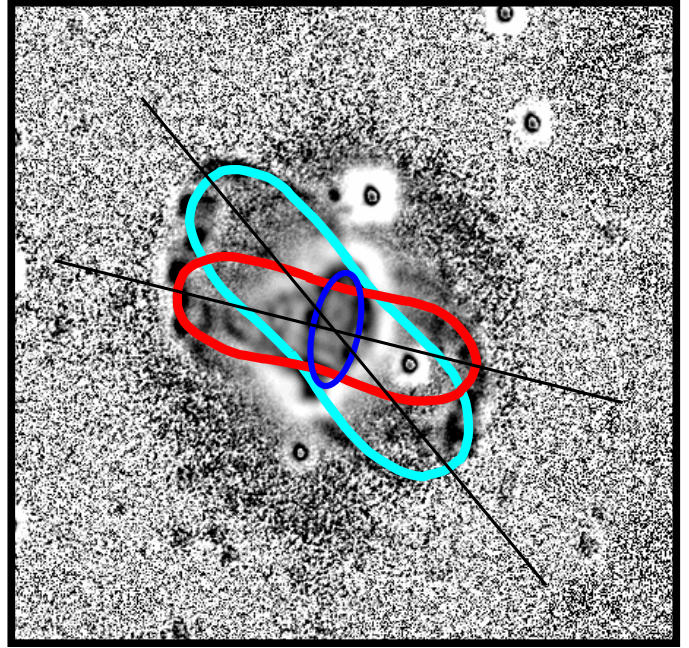


**Fig. 7.** NGC 6309 and the two bipolar outflows model. The fit of two hour-glass models is overlaid on the [O III] unsharp-masking image presented before. The central torus is also drawn.

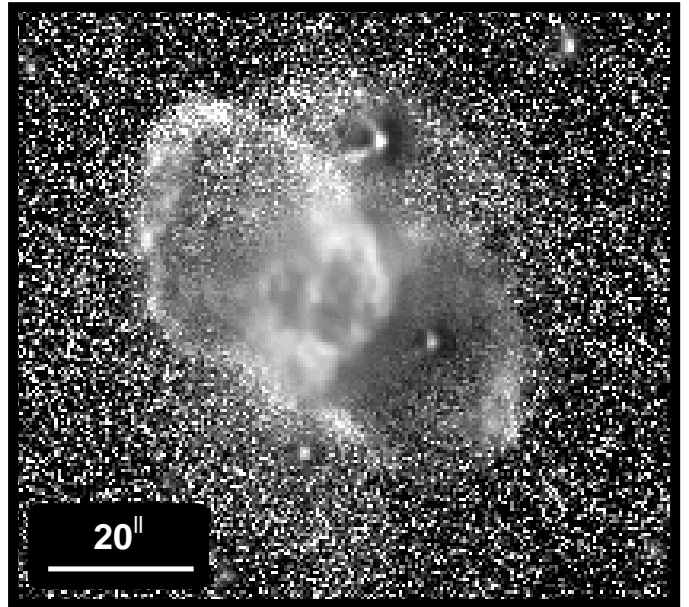


**Fig. 8.** [O III]/H $\alpha$  ratio image. White represents high values of the ratio.

[O III] emission is seen in the edge of the lobes, clearly related to the point-symmetric knots. It is noticeable that the emission vanished at the end of the SW lobe, possibly corresponding to a breaking of the shell due to the action of the outflow. According to Medina et al. (2007), the [O III] enhancement would be compatible with structures shaped by collimated outflows, as in the case of IC 4634. Finally, the circular halo probably corresponds to the remnant of the envelope ejected as a slow wind from the central star when it was at its AGB phase.



## 4. Conclusions

We have carried out an analysis of the planetary nebulae NGC 6309, based on ground-based and space-based imaging, high- and low-dispersion spectroscopy, as well as VLA-D radio continuum. We summarize the main conclusions of this work as follows.

NGC 6309 can be described as a quadrupolar PN formed by a bright central torus, two systems of bipolar lobes oriented at different directions, and point-symmetric knots that trace the edges of the lobes. The torus expands at  $25 \text{ km s}^{-1}$ , whereas the polar expansion velocity of the lobes is  $75 \text{ km s}^{-1}$  for a first bipolar system at PA  $76^\circ$ , and  $86 \text{ km s}^{-1}$  for another bipolar system at PA  $40^\circ$ . Assuming a distance of 2 kpc for the nebula, the kinematic ages of the structures ranges from 3700 to 4000 yr, suggesting that they have been formed in a short time span. The knots at the edges of the lobes suggest that the lobes have been formed by rapidly precessing bipolar jets that carved cavities in the previous red giant envelope. In addition to these structures, we detect a circular halo surrounding the torus and bipolar lobes, which probably corresponds to the envelope ejected in the AGB phase by the central star. There is also a conelike structure embedded in one of the lobes and with its base on the torus.

We also study internal variations of the physical conditions and chemical abundances in NGC 6309. The low-dispersion spectra indicate a high-excitation nebula, with low to medium variations of its internal physical conditions ( $10,600 \text{ K} \lesssim T_e[\text{O III}] \lesssim 10,900 \text{ K}$ ;  $10,100 \text{ K} \lesssim T_e[\text{N II}] \lesssim 11,800 \text{ K}$ ;  $1440 \text{ cm}^{-3} \lesssim N_e[\text{S II}] \lesssim 4000 \text{ cm}^{-3}$ ;  $1700 \text{ cm}^{-3} \lesssim N_e[\text{Cl III}] \lesssim 2600 \text{ cm}^{-3}$ ;  $1000 \text{ cm}^{-3} \lesssim N_e[\text{Ar IV}] \lesssim 1700 \text{ cm}^{-3}$ ). The radio continuum emission indicates a mean electron density of  $\approx 1900 \text{ cm}^{-3}$ ; emission measure of  $5.1 \times 10^5 \text{ pc cm}^{-6}$ ; and an ionised mass  $M(\text{H II}) \approx 0.07 M_\odot$ . The logarithmic extinction coefficient  $c_{\text{H}\beta}$  range from 0.70 to 0.97 (mean value 0.87), which probably is produced by differences in the internal dust distribution.

*Acknowledgements.* RV, SA, LO, MEC, and PFG were supported by grants 32214-E and 45848 (CONACYT), and by grants IN114199 and IN111903-3 (PAPIIT-DGAPA-UNAM). LFM and SA were supported by grant AYA2005-01495 of the Spanish MEC (cofunded by FEDER funds). JMT acknowledges partial financial support from the Spanish grant AYA2005-08523-C03. We are grateful to the staff of all the astronomical facilities used in this research, namely: (a) Centro Astronómico Hispano-Alemán, (b) Very Large Array of National Radio Astronomy Observatory, (c) Hubble Space Telescope Data Archive, (d) Observatorio Astronómico Nacional, operated by Universidad Nacional Autónoma de México, and (e) Observatorio de Sierra Nevada (IAA-CSIC). We thank the anonymous referee for critically reading the manuscript and for useful suggestions. We also thank fruitful discussions with Dr. Martín A. Guerrero (IAA-CSIC) and Prof. Mauricio Tapia (IA-UNAM). This research has made use of the SIMBAD database, operated at CDS, Strasbourg, France.

## References

- Amuel, P. R., Guseinov, O. H., Novruzova, H. I., Rustamov, Y. S. 1984, *Ap&SS*, 107, 19
- Armour, M. H., Kingsburgh, R. L. 2001, *RevMexAASC*, 10, 38
- Balick, B. 1987, *AJ*, 94, 671
- Briggs, D. S. 1995, PhD thesis, New Mexico Inst. of Mining and Technology
- Cliffe, J. A., Frank, A., Livio, M., Jones, T. W. 1995, *ApJ*, 447, L49
- Cahn J. H., Kaler J. B., Stanghellini L. 1992, *A&AS*, 94, 399
- Condon J. J., Kaplan L. D., 1998, *ApJS*, 117, 361
- Corradi, R. L. M., Schwarz, H. E. 1995, *A&A*, 293, 871
- Daub, C.T. 1982, *ApJ*, 260, 612
- García-Segura, G., López, J. A. 2000, *ApJ*, 544, 336
- Gonçalves, D. R., Corradi, R. L. M., Mampaso, A., Perinotto, A. 2003, *ApJ*, 597, 975
- Gonçalves, D. R., Ercolano, B., Carnero, A., Mampaso, A., Corradi, R. L. M. 2006, *MNRAS*, 365, 1039

- Górny, S. K., Stasinska, G., Escudero, A. V., Costa, R. D. D. 2004, *A&A*, 427, 231
- Grevesse, N., Asplund, M., Sauval, A. J. 2007, *Space Sci. Rev.*, 130, 105
- Howarth, I. D. 1983, *MNRAS*, 203, 301
- Icke, V. 1988, *A&A*, 202, 177
- Kahn, F. D. & West, K. A. 1985, *MNRAS*, 2012, 837
- Kingsburgh, R. L. & Barlow, M. J. 1994, *MNRAS*, 295, 75
- Kwok, S., Purton, C. R., Fitzgerald, P. M. 1978, *ApJ*, 219, L125
- Kwok, S. 2000, *The origin and evolution of planetary nebulae*. Cambridge; New York: Cambridge University Press, 2000. (Cambridge astrophysics series; 33)
- Lee, T.-H., Kwok, S. 2005, *ApJ*, 632, 340
- Livio, M., Pringle, J. E. 1996, *ApJ*, 465, L55
- Livio, M., Pringle, J. E. 1997, *ApJ*, 486, 835
- López, J. A., Meaburn, J., Palmer, J. W. 1993, *ApJ*, 415, L135
- López, J. A., Vázquez, R., Rodríguez, L. F. 1995, *ApJ*, 455, L63
- Maciel, W.J. 1984, *A&AS*, 55, 253
- Mellema, G. 1995, *MNRAS*, 277, 173
- Medina, J. J., Guerrero, M. A., Luridiana, V., Miranda, L. F., Riera, A., Velázquez, P. F. 2007, in “Asymmetrical Planetary Nebulae IV”, eds. R. L. M. Corradi, A. Manchado, & N. Soker, Proceedings in electronic book (reference will be published in ADS).
- Mezger, P. G., Henderson, A. P. 1967, *A&A*, 147, 471
- Milne, D.K., Aller, L.H. 1982, *A&AS*, 50, 209
- Miranda, L. F., Solf, J. 1992 *A&A*, 260, 397
- Miranda, L. F., Ayala, S., Vázquez, R., Guillén, P. F. 2006 *A&A*, 456, 591
- Peimbert, M. 1978, in *Planetary Nebulae*, IAU Symp. 76, ed. Y. Terzian, (Dordrecht: Reidel), 215
- Perinotto, M., Schönberner, D., Steffen, M., Calonaci, C. 2004, *A&A*, 414, 993
- Phillips, J.P., Pottasch, S.R. 1984, *A&A*, 130, 91
- Ratag, M.A., Pottasch, S.R. 1991, *A&AS*, 91, 481
- Rijkhorst, E.-J., Icke, V., Mellema, G. 2004, in “Asymmetrical Planetary Nebulae III” editors M. Meixner, J. Kastner, N. Soker, & B. Balick, ASP Conf. Series, 313, p.472
- Rijkhorst, E.-J. Mellema, G. & Icke, V. 2005, *A&AS*, 444, 849
- Sabbadin, F. 1984, *A&AS*, 58, 273
- Sahai, R., Trauger, J. T. 1998, *AJ*, 116, 1357
- Sahai, R., Le Mignant, D., Sánchez-Contreras, C., Campbell, R. D., Chaffee, F. H. 2005, *ApJ*, 622, L53
- Sánchez-Contreras, C., Le Mignant, D., Sahai, R., Chaffee, F. H., Morris, M. 2006 in IAU Symp 234, *Planetary Nebulae in our Galaxy and Beyond*, eds. M.J. Barlow & R.H. Mendez, Cambridge University Press, pp. 71
- Schneider, S. E., Terzian, Y., Purgathofer, A., Perinotto, M. 1983, *ApJS*, 52, 399
- Schwarz, H. E., Corradi, R. L. M., Melnick, J. 1992, *A&AS*, 96, 23
- Shaver, P. A., McGee, R. X., Newton, L. M., Danks, A. C., Pottasch, S. R. 1983, *MNRAS*, 204, 53
- Schönberner, D., Jacob, R., Steffen, M., Perinotto, M., Corradi, R. L. M., Acker, A. 2005, *A&A*, 431, 963
- Schönberner, D., Jacob, R., Steffen, M., Sandin, C. 2007, *A&A*, 473, 467,
- Solf, J., Ulrich, H. 1985, *A&A*, 148, 274
- Stanghellini, L., Corradi, R. L. M., Schwartz, H. E. 1993, *A&A*, 276, 463
- Vázquez, R., López, J. A., Miranda, L. F., Torrelles, J. M., Meaburn, J. 1999a, *MNRAS*, 308, 939
- Vázquez, R., Torrelles, J. M., Rodríguez, L. F., Gómez, Y., López, J. A., Miranda, L. F. 1999b, *ApJ*, 515, 633
- Vázquez, R., Miranda, L. F., Torrelles, J. M., Olguín, L., Benítez, G., Rodríguez, L. F., López, J. A. 2002, *ApJ*, 576, 860

## List of Objects

- ‘NGC 6309’ on page 1
- ‘NGC 6309’ on page 1
- ‘NGC 6309’ on page 2
- ‘IC 5217’ on page 3
- ‘Fleming 1’ on page 8
- ‘IC 4634’ on page 8

**Table 1.** Dereddened spectra and physical conditions from different regions in NGC 6309. Intensity values are relative to  $I_{H\beta}=100$ . Extinction law ( $f_\lambda$ ) is from Howarth (1983). The size of the integration region (in arcsec) along the slit is 7''.4 for **R1**, **R2**, **R3**, and **R4**, and 5''.3 for the rest. Slit width was set at 1''.6 in all the cases.

| Ion                              | $\lambda_0$ (Å)     | $f_\lambda$ | R1               | R2               | R3     | R4     | E2    | W1    | W2    |
|----------------------------------|---------------------|-------------|------------------|------------------|--------|--------|-------|-------|-------|
| [O II]                           | 3727                | 0.256       | 108              | 102              | —      | —      | —     | —     | —     |
| [Ne III]                         | 3869                | 0.230       | 163              | 165              | —      | —      | —     | —     | —     |
| [Ne III]                         | 3968                | 0.210       | 68               | 67               | —      | —      | —     | —     | —     |
| [S II]                           | 4071                | 0.189       | 6.5              | —                | —      | —      | —     | —     | —     |
| H $\delta$ + He II               | 4101                | 0.182       | 33               | 34               | —      | —      | —     | —     | —     |
| H $\gamma$                       | 4340                | 0.127       | 55               | 53               | 26     | 27     | 52    | —     | —     |
| [O III]                          | 4363                | 0.121       | 12               | 12               | 7.9    | 8.5    | —     | —     | —     |
| He I                             | 4471                | 0.095       | 8.2              | 7.1              | 3.4    | 3.2    | —     | —     | —     |
| He II                            | 4540                | 0.078       | —                | —                | 2.8    | 3.3    | —     | —     | —     |
| N III                            | 4640                | 0.054       | 4.3              | 5.0              | 5.2    | 6.1    | —     | —     | —     |
| He II                            | 4686                | 0.043       | 29               | 31               | 81     | 79     | 86    | 106   | —     |
| [Ar IV]                          | 4711                | 0.037       | 6.0              | 5.8              | 12     | 12     | —     | —     | —     |
| [Ar IV]                          | 4740                | 0.030       | 4.6              | 4.6              | 9.4    | 9.3    | —     | —     | —     |
| H $\beta$                        | 4861                | 0.000       | 100              | 100              | 100    | 100    | 100   | 100   | 100   |
| [O III]                          | 4959                | -0.024      | 487              | 464              | 335    | 365    | 341   | 364   | 451   |
| [O III]                          | 5007                | -0.036      | 1504             | 1466             | 993    | 1081   | 1046  | 1097  | 1238  |
| N I                              | 5199                | -0.082      | 0.9              | —                | —      | —      | —     | —     | —     |
| He II                            | 5411                | -0.133      | 2.5              | 2.3              | 6.2    | 6.0    | 8.5   | —     | —     |
| [Cl III]                         | 5517                | -0.154      | 1.1              | 1.0              | 0.7    | 0.7    | —     | —     | —     |
| [Cl III]                         | 5537                | -0.157      | 1.0              | 1.0              | 0.7    | 0.6    | —     | —     | —     |
| [N II]                           | 5755                | -0.195      | 1.0              | 1.0              | 0.6    | —      | —     | —     | —     |
| He I                             | 5876                | -0.215      | 13               | 12               | 7.1    | 8.1    | —     | —     | —     |
| [O I]                            | 6300                | -0.282      | 6.8 <sup>a</sup> | 7.2 <sup>a</sup> | 2.5    | 1.2    | —     | —     | —     |
| [S III]                          | 6312                | -0.283      | —                | —                | 1.8    | 1.7    | —     | —     | —     |
| [O I]                            | 6364                | -0.291      | 1.9              | 1.8              | 0.8    | 0.4    | —     | —     | —     |
| [Ar V]                           | 6435                | -0.302      | —                | —                | 1.4    | 1.4    | —     | —     | —     |
| [N II]                           | 6548                | -0.318      | 24               | 31               | 9.3    | 4.7    | —     | —     | —     |
| H $\alpha$                       | 6563                | -0.320      | 285              | 285              | 283    | 284    | 284   | 284   | 284   |
| [N II]                           | 6583                | -0.323      | 60               | 60               | 27     | 12     | 8.8   | —     | —     |
| He I                             | 6678                | -0.336      | 3.4              | 3.6              | 2.4    | 2.6    | —     | —     | —     |
| [S II]                           | 6717                | -0.342      | 8.0              | 9.1              | 2.9    | 1.3    | —     | —     | —     |
| [S II]                           | 6731                | -0.344      | 11               | 12               | 4.8    | 2.1    | —     | —     | —     |
| [Ar V]                           | 7006                | -0.380      | —                | —                | 3.1    | 2.7    | —     | —     | —     |
| He I                             | 7065                | -0.387      | 3.1              | 3.1              | 1.9    | 2.0    | —     | —     | —     |
| [Ar III]                         | 7136                | -0.396      | 17               | 19               | 14     | 13     | 19    | 21    | 21    |
| [Ar IV]+[Fe II]                  | 7170                | -0.401      | 1                | —                | 0.9    | 0.3    | —     | —     | —     |
| He II                            | 7178                | -0.401      | —                | —                | 0.9    | 0.7    | —     | —     | —     |
| [O II]                           | 7320                | -0.419      | 5.6 <sup>b</sup> | 5.7 <sup>b</sup> | 2.3    | 1.4    | —     | —     | —     |
| [O II]                           | 7330                | -0.420      | —                | —                | 2.0    | 1.3    | —     | —     | —     |
| $c_{H\beta}$                     |                     |             | 0.96             | 0.97             | 0.70   | 0.80   | 0.86  | 0.85  | 0.97  |
| $\log I_{H\beta}$                |                     |             | -13.4            | -13.5            | -13.2  | -13.4  | -15.2 | -15.3 | -15.9 |
| $T_e$ [O III]                    | (K)                 |             | 10 800           | 10 900           | 10 700 | 10 600 | —     | —     | —     |
| $T_e$ [N II]                     | (K)                 |             | 10 300           | 10 100           | 11 800 | —      | —     | —     | —     |
| $N_e$ [S II]                     | (cm <sup>-3</sup> ) |             | 1800             | 1440             | 4000   | 3600   | —     | —     | —     |
| $N_e$ [Cl III]                   | (cm <sup>-3</sup> ) |             | 2100             | 2350             | 2600   | 1700   | —     | —     | —     |
| $N_e$ [Ar IV]                    | (cm <sup>-3</sup> ) |             | > 1000           | > 1500           | > 1700 | > 1500 | —     | —     | —     |
| $\log H\alpha$ /[N II]           |                     |             | 0.533            | 0.499            | 0.889  | 1.244  | —     | —     | —     |
| $\log H\alpha$ /[S II]           |                     |             | 1.182            | 1.142            | 1.565  | 1.913  | —     | —     | —     |
| $\log$ [O III]5007/H $\alpha$    |                     |             | 0.723            | 0.711            | 0.545  | 0.580  | —     | —     | —     |
| $\log \lambda 6717/\lambda 6731$ |                     |             | 0.748            | 0.792            | 0.603  | 0.623  | —     | —     | —     |

<sup>a</sup> This emission line is blended with [S III]6312Å.

<sup>b</sup> This emission line is blended with [O II]7330Å.

Mean uncertainties are  $\Delta c_{H\beta} = \pm 0.02$ ,  $\Delta T_e = \pm 500$  K,  $\Delta N_e = \pm 400$  cm<sup>-3</sup>.

**Table 2.** Ionic abundances of NGC 6309. In the case of ions with more than one transition, a flux-weighted average was performed. Electron temperature and density values of  $T_e = 10\,700$  K and  $N_e = 2400$  cm<sup>-3</sup> were used on the calculations.

| Ion              |                      | R1   | R2   | R3   | R4   | E2 <sup>a</sup> | W1 <sup>a</sup> | W2 <sup>a</sup> |
|------------------|----------------------|------|------|------|------|-----------------|-----------------|-----------------|
| He <sup>+2</sup> |                      | 0.02 | 0.03 | 0.07 | 0.06 | 0.06            | 0.09            | —               |
| He <sup>+</sup>  |                      | 0.09 | 0.09 | 0.05 | 0.06 | —               | —               | —               |
| O <sup>+2</sup>  | ( $\times 10^{-4}$ ) | 4.68 | 4.93 | 2.02 | 3.78 | 3.66            | 3.82            | 4.41            |
| O <sup>+</sup>   | ( $\times 10^{-5}$ ) | 4.70 | 5.93 | 1.28 | 2.16 | —               | —               | —               |
| O <sup>0</sup>   | ( $\times 10^{-5}$ ) | 1.13 | 1.29 | 0.27 | 0.25 | —               | —               | —               |
| Ar <sup>+4</sup> | ( $\times 10^{-7}$ ) | —    | —    | 4.26 | 5.83 | —               | —               | —               |
| Ar <sup>+3</sup> | ( $\times 10^{-7}$ ) | 8.78 | 9.22 | 12.2 | 19.4 | —               | —               | —               |
| Ar <sup>+2</sup> | ( $\times 10^{-6}$ ) | 1.48 | 1.68 | 0.90 | 1.18 | 1.71            | 1.91            | 1.92            |
| N <sup>+</sup>   | ( $\times 10^{-5}$ ) | 1.15 | 1.37 | 0.37 | 0.25 | 0.18            | —               | —               |
| N <sup>0</sup>   | ( $\times 10^{-6}$ ) | 2.18 | —    | —    | —    | —               | —               | —               |
| S <sup>+2</sup>  | ( $\times 10^{-6}$ ) | —    | —    | 2.14 | 3.99 | —               | —               | —               |
| S <sup>+</sup>   | ( $\times 10^{-7}$ ) | 5.29 | 5.87 | 2.07 | 1.31 | —               | —               | —               |
| Ne <sup>+2</sup> | ( $\times 10^{-4}$ ) | 1.59 | 1.75 | —    | —    | —               | —               | —               |
| Cl <sup>+2</sup> | ( $\times 10^{-7}$ ) | 1.28 | 1.28 | 0.63 | 0.92 | —               | —               | —               |

**Table 3.** Elemental abundances of NGC 6309. ICFs were obtained following Kingsburgh & Barlow (1994). Comparison with mean values of All-type PNe, Type I PNe and other objects are shown. Except for He, all the abundances relative to H are logarithmic values with H=+12.

| Ion  | R1          | R2          | R3          | R4          | G04 <sup>a</sup> | PNe <sup>b</sup> | TIPNe <sup>c</sup> | H II <sup>d</sup> | Sun <sup>e</sup> |
|------|-------------|-------------|-------------|-------------|------------------|------------------|--------------------|-------------------|------------------|
| He/H | 0.11 ± 0.01 | 0.11 ± 0.01 | 0.12 ± 0.01 | 0.12 ± 0.01 | 0.10 ± 0.01      | 0.12 ± 0.02      | 0.13 ± 0.04        | 0.10 ± 0.01       | 0.09 ± 0.01      |
| O/H  | 8.74 ± 0.02 | 8.72 ± 0.02 | 8.72 ± 0.01 | 8.74 ± 0.01 | 8.64 ± 0.02      | 8.68 ± 0.15      | 8.65 ± 0.15        | 8.70 ± 0.04       | 8.66 ± 0.05      |
| N/H  | 7.93 ± 0.02 | 7.92 ± 0.02 | 8.04 ± 0.01 | 7.89 ± 0.02 | 8.20 ± 0.12      | 8.35 ± 0.25      | 8.72 ± 0.15        | 7.57 ± 0.04       | 7.78 ± 0.06      |
| Ne/H | 8.26 ± 0.02 | 8.25 ± 0.02 | —           | —           | 7.82 ± 1.00      | 8.09 ± 0.15      | 8.09 ± 0.15        | 7.90 ± 0.10       | 7.84 ± 0.06      |
| Ar/H | 6.40 ± 0.10 | 6.42 ± 0.10 | 6.54 ± 0.01 | 6.51 ± 0.01 | —                | 6.39 ± 0.30      | 6.42 ± 0.30        | 6.42 ± 0.04       | 6.18 ± 0.08      |
| S/H  | 6.74 ± 0.01 | 6.73 ± 0.01 | 6.84 ± 0.01 | 6.87 ± 0.01 | 6.49 ± 0.05      | 6.92 ± 0.30      | 6.91 ± 0.30        | 7.06 ± 0.06       | 7.14 ± 0.05      |

<sup>a</sup> Taken from Górny et al. (2004).

<sup>b</sup> Average for PNe (Kingsburgh & Barlow 1994).

<sup>c</sup> Average for Type I PNe (Kingsburgh & Barlow 1994).

<sup>d</sup> Average for H II regions (Shaver et al. 1983).

<sup>e</sup> The Sun (Grevesse, Asplund, & Sauval 2007).